

Formation of a three-dimensional bottle beam via an engineered microsphere

YAN ZHOU  AND MINGHUI HONG*

Department of Electrical and Computer Engineering, National University of Singapore, Singapore 117576, Singapore

*Corresponding author: elehnh@nus.edu.sg

Received 30 April 2021; revised 26 June 2021; accepted 26 June 2021; posted 28 June 2021 (Doc. ID 430514); published 30 July 2021

In this work, we propose a novel approach to produce three-dimensional (3D) optical trapping with sub-wavelength size through an engineered microsphere, under linear polarization states of an incident light. The engineered microsphere is designed to contain the segmented regions of diffractive patterns and made by focused ion beam fabrication. We simulate and experimentally characterize the focus performance of the engineered microsphere. The emitted light field from the exit surface of the engineered microsphere forms a pair of axially arranged focused beams, and they are connected with a continuous optical field embracing a 3D optical null at the center, forming the so-called optical bottle beam. Experimental results and numerical simulation are in good agreement. Such micro-optics can be used for precise and localized optical trapping. © 2021 Chinese Laser Press

<https://doi.org/10.1364/PRJ.430514>

1. INTRODUCTION

Optically trapping and translating particles using focused laser beams has become the technology for non-contact manipulation of microscopic objects, with extensive impacts on applications ranging from optics, thermodynamics, biology, and atomic physics [1–8]. Conventional optical tweezers use high-numerical-aperture ($NA > 0.8$) lenses to generate a stable gradient trapping potential [3], which are bulky and of high cost; they also suffer from a lack of flexibility and integrated ability, poor remote operating capability, and demand for large-volume infrastructure. As an alternative, optical fiber-based tweezers have also been developed in the form of paired and counter-aligned fibers or a tapered/patterned fiber [9–13], but they offer limited control over the light field, and yet they are not suitable for large-scale integration. Another field of approaches is on-chip devices, including planar photonic devices, such as optical waveguides [14–16], plasmonic structures [17–19], and optical resonators [20–22], and has been proposed for on-chip trapping. These devices utilize evanescent waves to produce the optical-gradient potential, which only allows particle manipulation in two dimensions at immediate proximity of the chip surface due to the stringent decay length of evanescent fields.

Stable and robust optical trapping demands a strong gradient force along three spatial directions (XYZ) to provide a sufficient trapping force in the radial direction and counter-balance the scattering force along the axial direction. One structured light beam called the “bottle beam” contains volumes of low (zero) intensity surrounded by the high-intensity regions, providing efficient means for the 3D particle localization and controllable displacement [23–27]. Such beams can be

generated, e.g., by the superposition of oppositely propagating optical vortex beams [25] or inside the focal volume of a lens with a controlled spherical aberration [26]. Generation of such beam structures usually relies on a combination of complex optics [24,25]. In many cases, the resulted optics traps are of sizes from the micrometer to millimeter range [26,27], so one trap can contain a cluster of micro/nanoparticles with Brownian motions, which is not favored for isolated trapping. As such, the generation of the gradient optical trap from specially designed miniaturized optics can be a good alternative approach. Transparent microspheres are a class of refractive micro-optics possessing elegant light focusing with low loss and have proved to achieve various performances in nano-patterning and nano-imaging [28–31]. With the help of engineered nanostructures on the microsphere, further configuration of the focused light field can be achieved to generate structured or tailored beams [32–37].

In this paper, we propose and demonstrate a novel design of micro-optics for optical trapping, whose functionality is based on the refractive microsphere decorated with spatially variant diffractive patterns, to generate a structured beam with a 3D void space as the gradient optical trap, or an “optical bottle.” The spatially variant diffraction pattern is made from segmented annular rings taken from Fresnel zone plate (FZP) designs. Unlike conventional FZP patterns, each segment ring has its center of curvature dislocated from the optical axis in the transverse plane (perpendicular to the light propagation axis). Region-selective manipulation of light, from each part of the hybrid diffraction patterns, couples with the strong light focusing of the microsphere body and forms a bottle beam with near

or sub-wavelength void space as the optical trap. This novel design of micro-optics is ideally suited for integrated optical tweezers benefiting from several unique features. First, this design enables the precise positioning of the trap location in the 3D region above the micro-optics and facile adaptations of the trapping potential. Second, compared to other planar devices used for free-space outcoupling, such as diffractive gratings, plasmonic scatterers, and metasurfaces, refractive-based micro-optics offers excellent optical efficiency and broadband operation. The high efficiency enables a low trapping threshold power, whereas the large spectral bandwidth is favored for fluorescence or Raman excitation. Micro-optics can be seamlessly integrated with on-chip waveguides and interfaced with photonic integrated circuits to include new functionalities, such as dynamic tuning of optical traps. In the following, we will present the design, fabrication, and characterization of two embodiments of the engineered microspheres.

2. DESIGN AND METHOD

In this paper, the core idea of this design is to incorporate the focusing of light by the refractive microsphere body and light

manipulation by the diffractive pattern on the truncated surface of the engineered microsphere. The resulted optical bottle beam comprises two axial foci and a center-hollowed region connecting the two focal beams, as seen in Fig. 1(a). The two foci are generated from the diffraction pattern as designed, while the interconnecting region of the light field is formed from two sources. The first source is the deliberately uncompensated spherical aberration of the truncated microsphere, and the second source is attributed to the centers of curvature of all segment zones being dislocated from the optical axis.

For microspheres with diameters larger than 10λ , they exhibit substantial spherical aberration when light propagation is not restricted to a small fraction of its cross section. In the geometric optics regime, for positive spherical aberration, the light rays close to the optical axis intersect it near the paraxial focus position. As the ray height at the lens increases, the position of the ray intersection with the optical axis moves farther away from the paraxial focus towards the lens. In a carefully aligned system, the only significant distortion is the one introduced by primary (i.e., third-order) spherical aberration. Assuming plane wave light illuminates from the spherical

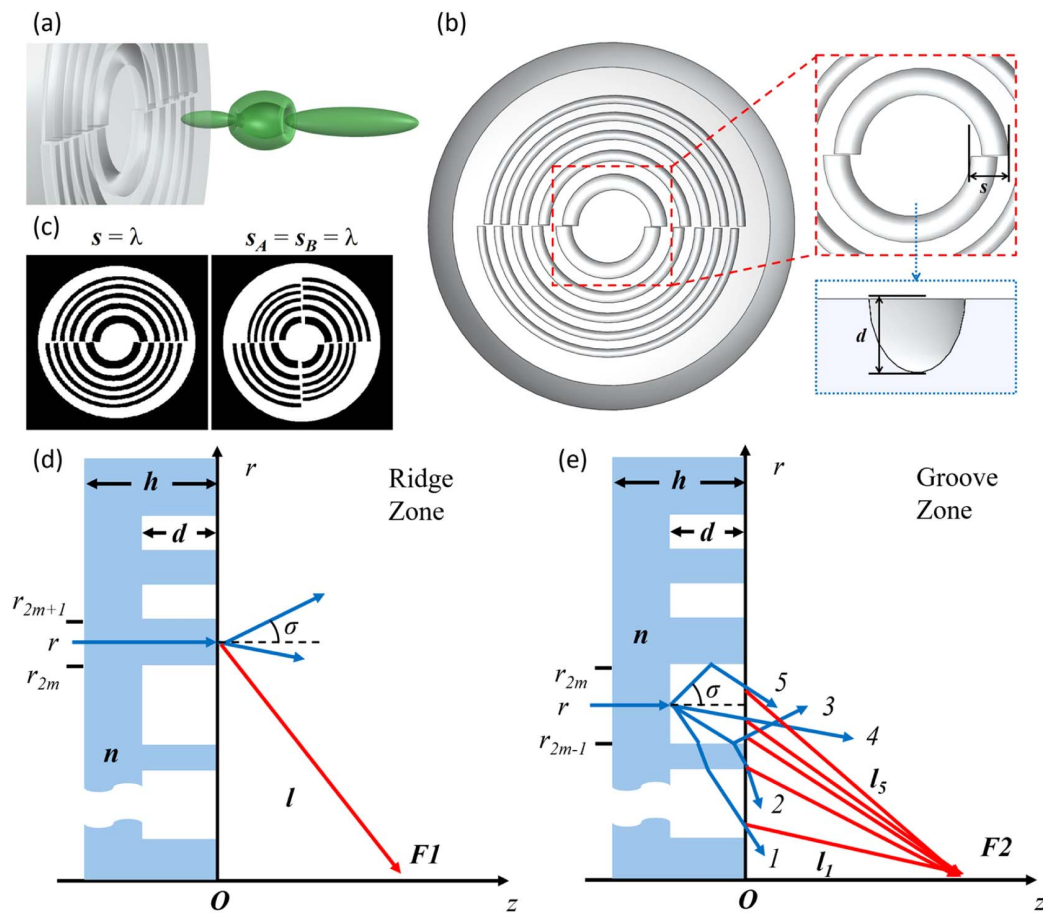


Fig. 1. Conceptual design of engineered microsphere patterned with the segmented Fresnel annular zones. (a) 3D sketch of optical bottle beam (green) generated from the engineered microsphere. (b) Schematic sketch of the two-segment zone design engineered microsphere, s in the upper inset denotes the total relative dislocation of the opposite segments from the optical axis, while d in the lower inset is the etched depth of the annular zone with an elliptical cross section. (c) Refractive index maps show two embodiments of segmented regions (left: two-segment; right: four-segment), and all total relative dislocation distances are equal to λ . The light scattering by the piecewise interface of a phase FZP and related geometric parameters for (d) ridge zones and (e) groove zones. Sketches in (d) and (e) are not drawn to scale.

surface of the truncated microsphere, its Coddington shape and position factors are both equal to -1 . The aberration function φ , which defines the deviation of the distorted wavefront from the ideal convergent spherical wavefront, can be well approximated by [38]

$$\varphi = -\frac{n^2 r^4}{8f^3(n-1)^2}, \quad (1)$$

where $n \sim 1.56$ is the refractive index of the microsphere, r is the radial distance from the optical axis, and f is the focal distance. The third-order spherical aberration (Seidel) coefficient for an ideal ball lens is given as [39]

$$S_I = \frac{n}{4(n-1)^2} - \frac{1}{4}, \quad (2)$$

while the Seidel coefficient for field curvature or the Petzval coefficient is equal to one.

As described in previous literature, we deal with the monochromatic field whose temporal behavior is described by the factor $\exp(i\omega t)$, which, as usual, is omitted in the subsequent expressions [40]. We also consider the beams with linear polarization, which can be described by the scalar model. Then, the electric fields of a plane wave and a Gaussian beam propagating along the z axis are described by the complex amplitude distributions:

$$A_{pl} = \exp(ikz), \quad (3)$$

and

$$A_G = \frac{w_0}{w(z)} \exp\left[-\frac{\rho^2}{w^2(z)}\right] \times \exp\left\{i\left[kz + \frac{k\rho^2}{2R(z)} - \arctan \frac{z-z_0}{z_R}\right]\right\}, \quad (4)$$

respectively, where z_0 denotes the position of the beam waist, w_0 is the waist radius, the current beam radius is $w(z) = w_0 \cdot [1 + (z-z_0)^2/z_R^2]^{1/2}$, $z_R = \pi w_0^2/\lambda$ is the Rayleigh length, λ is the wavelength of light, $\rho = (x^2 + y^2)^{1/2}$ is the cylindrical coordinate, $k = 2\pi/\lambda$ is the wave number, and the wavefront curvature radius $R(z) = (z-z_0)[1 + z_R^2/(z-z_0)^2]$.

The intensity distribution in the focal region of a lens illuminated with a Gaussian beam may be found by evaluating the scalar Debye integral, which is based on the Huygens–Fresnel principle and uses the boundary conditions approximated by the Kirchhoff diffraction theory [40]. The spatial variation of the intensity I is then

$$I(u, v) = \frac{8\pi\alpha^4 P}{\lambda^2 f^2 w_0^2} \left| \int_0^1 \exp\left(-\frac{\zeta^2}{w^2}\right) \exp\left[-i\left(k\varphi - \frac{u\zeta^2}{2}\right)\right] J_0(v\zeta) \zeta d\zeta \right|^2, \quad (5)$$

where $w = w_0/\alpha$ is the reduced radius of the beam waist, α is the radius of the entrance aperture of the microsphere, $\zeta = r/\alpha$, P is the beam power, J_0 is a Bessel function of the first kind of order zero, and the coordinates u and v are defined as $u = kz(\alpha/f)^2$ and $v = kr(\alpha/f)$.

In the design, several key parameters can directly influence the beam formation. These parameters include the size,

material (refractive index) and depth of the truncation of microsphere, wavelength of the coherent illumination light, and diffraction patterns. To be more specific on the diffraction pattern, it is made of segmented phase type FZP annular zones, each segment region has its center of curvature dislocated a distance of $s/2$ from the optical axis, and, within one segment region, all grooves have the same etching depth d , as seen in Fig. 1(b). After the segmented annular zones are fabricated on the truncated microsphere, the etched parts are called the groove zones, and the unstructured ring-shape zones in between those grooves are called the ridge zones, as seen in Figs. 1(d) and 1(e). Light emitted from the ridge and groove zones is manipulated in a way that they arrive at different axial positions on the optical axis, forming two distinct focal beams. In our design, the first focal beam (F1), which is located near the exit surface of engineered microsphere, is largely contributed by the ridge zones; the second focal beam (F2) is mainly attributed to the groove zones. Taking f_d as the designed focal length, the FZP zone boundaries are written as

$$r_m = \sqrt{mf_d\lambda + (m\lambda/2)^2}, \quad m = 1, 2, 3, \dots, 2N + 1, \quad (6)$$

where N is the etched zone number.

For the incident light passing through each ridge zone, the left side of Fig. 1(d) shows the scattering of transmitted light at the interface of $z = 0$ due to the finite size of a ridge. The source field components of the ridge zone are the superposition of scattering light over the range of scattering angle σ . Assuming that with cylindrical coordinates (ρ, η, z) and applying the Rayleigh–Sommerfeld integral, we can obtain the diffraction field of the FZP's ridge zones [41]:

$$\begin{aligned} E_x^{\text{rid}}(\rho, \eta, z) &= -\frac{z}{2\pi} \sum_{m=0}^N \int_{r_{2m}}^{r_{2m+1}} \int_0^{2\pi} \int_{-\pi/2}^{\pi/2} E_{0x}^{\text{rid}}(r, \varphi; \sigma) \frac{ikl-1}{l^3} \\ &\quad \times \exp(ikl) r dr d\varphi d\sigma, \\ E_y^{\text{rid}}(\rho, \eta, z) &= -\frac{z}{2\pi} \sum_{m=0}^N \int_{r_{2m}}^{r_{2m+1}} \int_0^{2\pi} \int_{-\pi/2}^{\pi/2} E_{0y}^{\text{rid}}(r, \varphi; \sigma) \frac{ikl-1}{l^3} \\ &\quad \times \exp(ikl) r dr d\varphi d\sigma, \\ E_z^{\text{rid}}(\rho, \eta, z) &= \frac{z}{2\pi} \sum_{m=0}^N \int_{r_{2m}}^{r_{2m+1}} \int_0^{2\pi} \int_{-\pi/2}^{\pi/2} [(\rho \cos \eta - r \cos \varphi) \\ &\quad \times E_{0x}^{\text{rid}}(r, \varphi; \sigma) (\rho \sin \eta - r \sin \varphi) \\ &\quad \times E_{0y}^{\text{rid}}(r, \varphi; \sigma)] \frac{ikl-1}{l^3} \\ &\quad \times \exp(ikl) r dr d\varphi d\sigma, \end{aligned} \quad (7)$$

where $r_0 = 0$. The incoming light in the phase FZP's groove zones is scattered by the interface of $z = -d$. $E_{0x}^{\text{rid}}(r, \varphi; \sigma)$ and $E_{0y}^{\text{rid}}(r, \varphi; \sigma)$ are the scattering field components in the x and y directions, respectively. The transmitted scattering light in each groove zone is divided into five parts denoted by 1 to 5, as shown on the right side of Fig. 1(e), and other scattering light is neglected since their contributions to the diffraction field are limited. The diffraction field of the FZP's groove zones can be written as

$$\begin{aligned}
 E_{x,n}^{\text{gro}}(\rho, \eta, z) &= -\frac{z}{2\pi} \sum_{m=1}^N \int_{r_{2m-1}}^{r_{2m}} \int_0^{2\pi} \int_{\sigma_{n,1}}^{\sigma_{n,2}} E_{0x,n}^{\text{gro}}(r', \varphi; \sigma) \frac{ikl_n - 1}{j^3} \\
 &\quad \times \exp(ikl_n) r' \xi_n dr d\varphi d\sigma, \\
 E_{y,n}^{\text{gro}}(\rho, \eta, z) &= -\frac{z}{2\pi} \sum_{m=1}^N \int_{r_{2m-1}}^{r_{2m}} \int_0^{2\pi} \int_{\sigma_{n,1}}^{\sigma_{n,2}} E_{0y,n}^{\text{gro}}(r', \varphi; \sigma) \frac{ikl_n - 1}{j^3} \\
 &\quad \times \exp(ikl_n) r' \xi_n dr d\varphi d\sigma, \\
 E_{z,n}^{\text{gro}}(\rho, \eta, z) &= \frac{z}{2\pi} \sum_{m=1}^N \int_{r_{2m-1}}^{r_{2m}} \int_0^{2\pi} \int_{\sigma_{n,1}}^{\sigma_{n,2}} [(\rho \cos \eta - r' \cos \varphi) \\
 &\quad \times E_{0x,n}^{\text{gro}}(r, \varphi; \sigma) + (\rho \sin \eta - r' \sin \varphi) \\
 &\quad \times E_{0y,n}^{\text{gro}}(r, \varphi; \sigma)] \frac{ikl_n - 1}{j^3} \\
 &\quad \times \exp(ikl_n) r' \xi_n dr d\varphi d\sigma, \tag{8}
 \end{aligned}$$

where $l_n = [r'^2 + \rho^2 + z^2 - 2r\rho \cos(\varphi - \eta)]^{1/2}$, $\xi_n = dr'/dr$, and r' related to r in the interface of $z = -d$ is the radial coordinate in the diffraction screen of $z = 0$.

In this paper, two embodiments of engineered microspheres are studied. One is a two-segment design, and both segmented regions have identical parameters except that they face each other; with a total relative dislocation distance s , such embodiment is visually presented in Figs. 1(a)–1(c). The phase transformation introduced by the designed pattern can be defined as

$$\Phi(x, y) = \begin{cases} 2\pi - Kx, & y > 0 \\ \pi + Kx, & y \leq 0 \end{cases}, \tag{9}$$

where K is the phase-gradient parameter, and its exact form depends on the actual FZP design parameters.

The other is a four-segment asymmetric design containing four segmented regions [Fig. 1(c)], and the four regions can be separated into two pairs of opposite regions, namely, pairs A and B . Each opposite pair of regions has the same FZP design, while neighboring regions are of different parameters. The

phase transformation introduced by this design can be defined as

$$\Phi(x, y) = \begin{cases} 2\pi - K_A x, & x > 0, y > 0 \\ \pi + K_B x, & x > 0, y \leq 0 \\ \pi + K_A x, & x \leq 0, y \leq 0 \\ 2\pi - K_B x, & x \leq 0, y > 0 \end{cases}, \tag{10}$$

where K_A and K_B are the phase-gradient parameters for the two region pairs, and the exact forms depend on the actual FZP design parameters.

The vectorial light field is then simulated using a finite-difference time-domain (FDTD) solver (Lumerical FDTD). The truncated dielectric microsphere is set to face the illumination light with its spherical side surface, thus the shadow side surface is flat and decorated with the designed etch patterns. The microsphere used is set as borosilicate glass ($n = 1.56$ at 589 nm). As in the experimental setup, the laser beam used has a beam diameter (~ 1 mm) much larger than the microsphere (15–20 μm), quasi-plane wave approximation is applied, and the illumination source is set to be a linearly polarized plane wave (wavelength of 532 nm). The boundary condition in the FDTD region is set to be perfectly matched layers (PMLs), and a mesh size of $\lambda/10$ is applied within the entire simulation region.

As seen in Fig. 2, simulated Poynting vector distributions and 2D plots show the collective effect of manipulated beams from all engineered regions to form a “bottle beam.” By using a two-segment design with $s_A = s_B = \lambda$, where $\lambda = 532$ nm, an optical trap in the “bottle beam” is generated with sub-wavelength dimensions in both axial and transverse directions. The dimensions are determined by the direction with the lowest optical potentials. If the peak field intensity in the transverse direction, I_{Trans} , is smaller than that for any of the two foci located along the axial direction, I_{Ax} , the criterion of optical trap size $I < I_{\text{Trans}}/2$ applies for all directions inside the 3D trap region. This is because the particle trapping in a 3D space

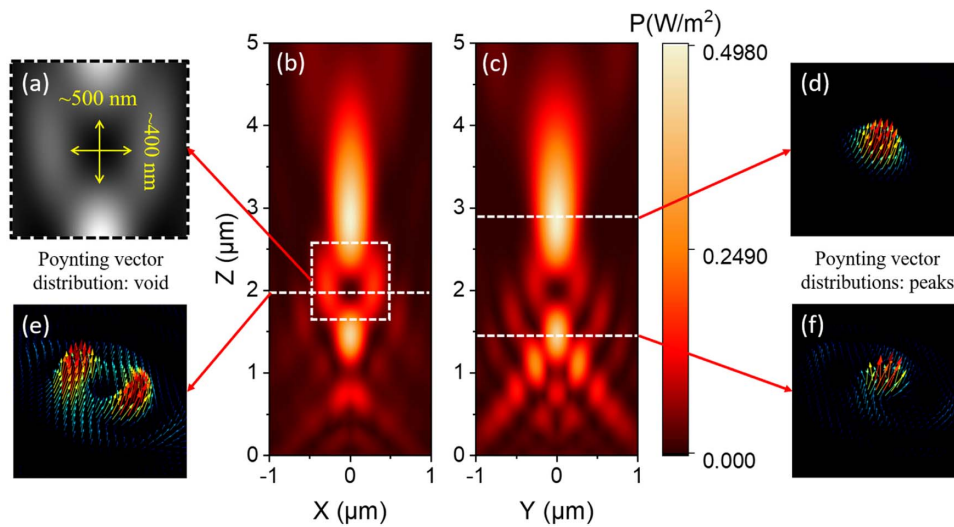


Fig. 2. “Bottle beam” generation via a two-segment design engineered microsphere from the view of Poynting vector distributions. (a) A zoomed view of the 3D optical trap with estimated axial and transverse dimensions, which are taken from the square and enclosed region in (b) XZ plane Poynting vector distribution. (c) YZ plane Poynting vector distribution. (d)–(f) The 3D Poynting vector plots taken from the three planes indicated in (b) and (c), where (e) is the optical trap or 3D void and (d) and (f) are the two foci.

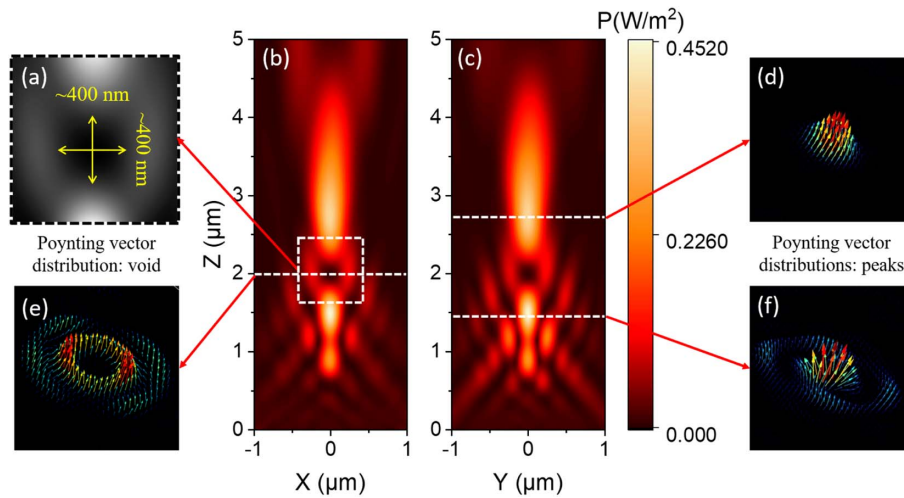


Fig. 3. “Bottle beam” generation via a four-segment design engineered microsphere from the view of Poynting vector distributions. (a) A zoomed view of the 3D optical trap with estimated axial and transverse dimensions, which are taken from the square and enclosed region in (b) XZ plane Poynting vector distribution. (c) YZ plane Poynting vector distribution. (d)–(f) The 3D Poynting vector plots taken from the three planes indicated in (b) and (c), where (e) is the optical trap or 3D void and (d) and (f) are the two foci.

relies on the lowest optical potential barrier around it, which in turn determines the power threshold of the laser beam. As expected from the spatially separate patterned regions, “twisted” beams are obvious from the Poynting vector plot at the first focus [Fig. 2(f)]. As the beams continue to propagate, their twisting is still easy to be identified at an observation plane in the optical trap region [Fig. 2(e)]. When light propagates further, beam interference occurs, and thus the beam twisting becomes less remarkable when they meet again at the optical axis to form the second focus, as seen in Fig. 2(d).

Similar to Fig. 2, simulated Poynting vector distributions and 2D plots in Fig. 3 show the “bottle beam” formation from all patterned regions of a four-segment engineered microsphere with $s_A = s_B = \lambda$. Again, a “bottle beam” is generated with an optical trap of sub-wavelength dimensions in both the axial and transverse directions. Obvious “beam twisting” is observed at the first focus [Fig. 3(f)]. At an observation plane in the optical trap region, beam twisting is still discernible by looking at the Poynting vector distribution [Fig. 3(e)]. However, compared to Fig. 2(e), Poynting vectors around the optical null region possess significantly smaller amplitude variations. At this plane, such amplitude variations are mitigated due to partial interference of light beams emerging from the four smaller spatially variant segmented regions with alternate parameters. When light propagates further, beam interference occurs, and thus the beam twisting becomes less remarkable when they meet again at the optical axis to form the second focus, as seen in Fig. 3(d).

Figure 4 shows a detailed insight by checking phase distributions at the same observation plane from the exit surface for both two- and four-segment designs. For the two-segment case, the mutually dislocated regions act as two sources of manipulated light beams. From x and y component phase distributions in the upper row of Fig. 3, the phase origin from two beam sources is still identified near the optical axis. As for the four-segment design, it is clear to see that it offers E -field phase

singularities in transverse directions, enabling a “3D pocket” with more uniform intensity distributions in transverse planes. Both the z component phase maps indicate the spiral-like propagation of beam vectors along the optical axis, while the four-segment design (lower row) results in a narrower distribution of the longitudinal component.

To conduct light field distribution characterization, borosilicate glass microspheres (Thermal Fischer, diameter $\sim 20 \mu\text{m}$) are truncated to become hyper-hemispheres using a focused ion beam (FIB) system (GAIA, TESCAN). The two designed patterns (two- and four-segment) are etched on the flat surfaces of the truncated microspheres using the same FIB system. The radius of curvature for the unstructured surface of the Fresnel zone microspheres (FZMS) is $9.5\text{--}11.0 \mu\text{m}$. Each of the fabricated engineered microspheres is located within a mesh on a copper transmission electron microscopy (TEM) grid (Ted Pella, thickness $\sim 5 \mu\text{m}$), with its lower waist mechanically held and supported during all experiments. During the FIB fabrication, the depth of truncation D_T of the microsphere is regularly monitored by measuring the radius R_m of the milled flat surface. The value of D_T can be calculated using simple trigonometry $R^2 = R_m^2 + (R - D_T)^2$, where R is the radius of the original microsphere. The effect of the D_T/R ratio on the beam formation and the optimization process has been discussed in our previous work [36]. To monitor groove depths, before each sample fabrication, a testing sample (truncated microsphere) of the same material is used to adjust FIB parameters to etch grooves with a certain designed depth according to simulation settings.

3. RESULTS AND DISCUSSION

The microspheres engineered by FIB as seen in Figs. 5 and 6 are characterized with the experimental setup as described in the previous literatures using a commercial optical microscope system (Nikon Eclipse Ni-E) [35–37]. The linearly polarized

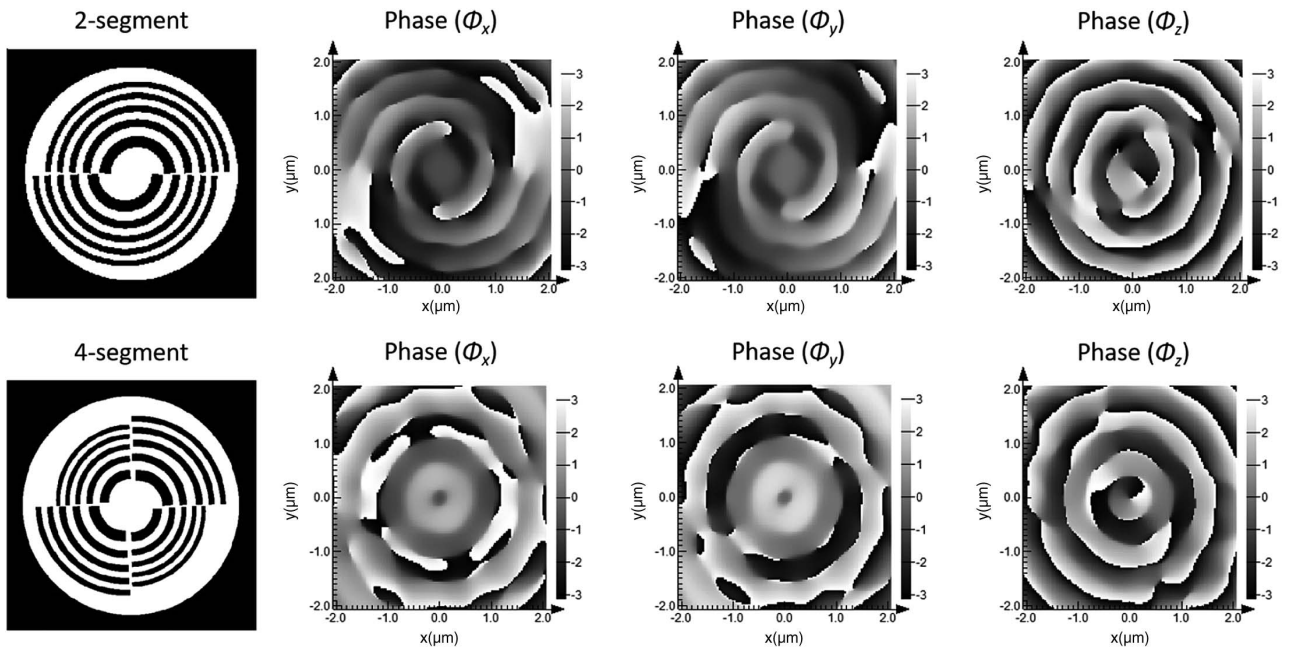


Fig. 4. Phase mapping for the designs at the same observation XY plane where the 3D void occurs, both cases are set at a 4λ distance from the exit surface. Upper row: x , y , and z phase distributions for the two-segment design; lower row: x , y , and z phase distributions for the four-segment design.

illumination beam is from a laser source (532 nm, MGL-FN-532, CNI Lasers) with a fixed controller voltage of 0.23 V in all experiments. The laser beam is directed to the spherical side of the engineered microspheres, is focused by the microsphere,

and exits from the patterned side to generate “bottle beams” along the optical axis. Fabricated microspheres are observed under a scanning electron microscope (SEM, TESCAN) as well as under an optical microscope (Nikon Eclipse Ni-E) equipped

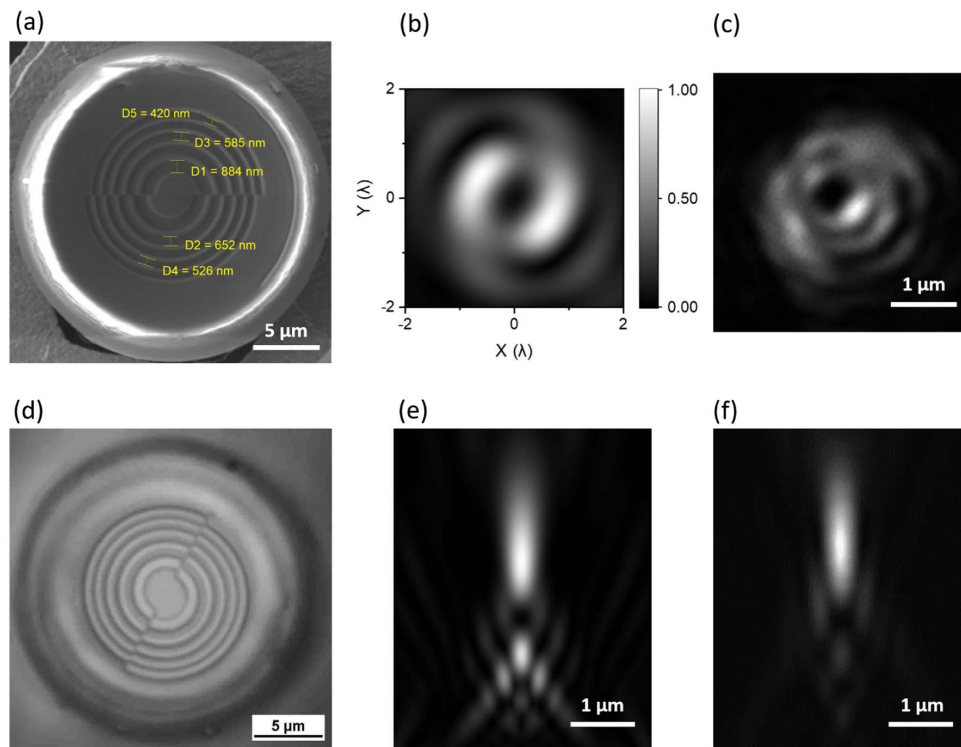


Fig. 5. Characterization of the fabricated two-segment design microsphere. Images of the fabricated microsphere are taken with (a) SEM and (d) optical microscope. Normalized FDTD-simulated light intensity field $|E|^2$ is plotted in (b) XY and (e) XZ planes, respectively. Measured light intensity fields are presented in (c) XY plane and (f) XZ plane. Scale bars: (a) and (d) 5 μm ; (c), (e), and (f) 1 μm .

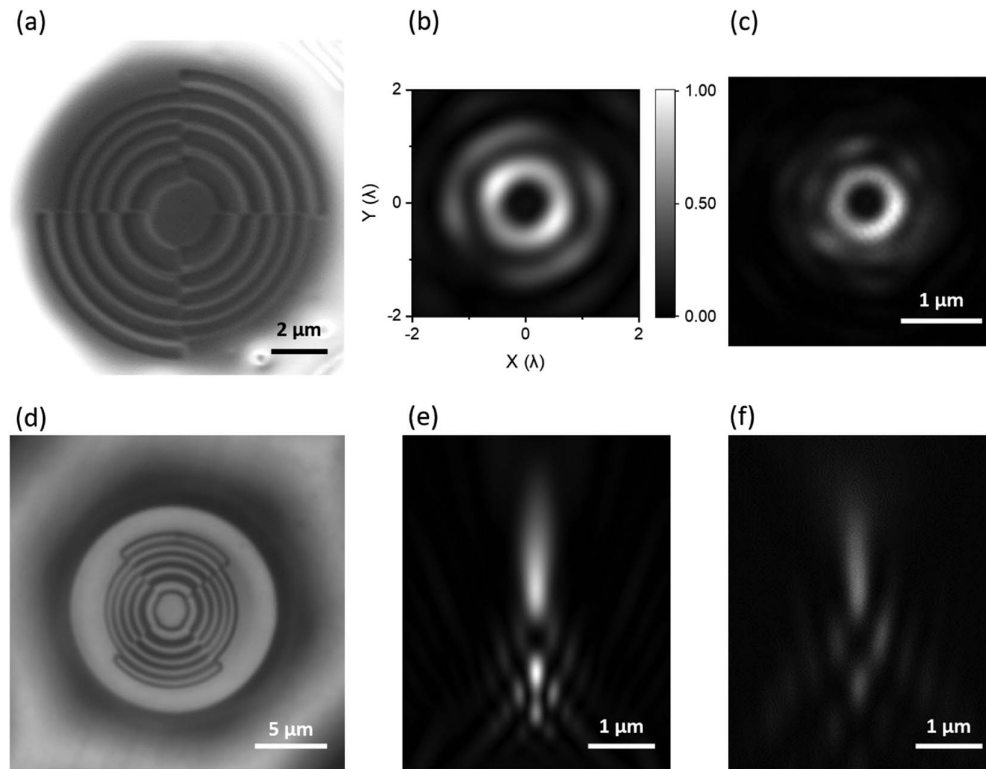


Fig. 6. Characterization of the fabricated four-segment design microsphere. Images of the fabricated microsphere are taken with (a) SEM and (d) optical microscope. Normalized FDTD-simulated light intensity field $|E|^2$ is plotted in (b) XY and (e) XZ planes, respectively. Measured light intensity fields are presented in the (c) XY plane and (f) XZ plane. Scale bars: (a) $2\ \mu\text{m}$; (d) $5\ \mu\text{m}$; (c), (e), and (f) $1\ \mu\text{m}$.

with a high-NA objective lens ($100\times$, NA 0.9). In Figs. 5 and 6, the characterization results are demonstrated and compared with the simulation results for two- and four-segment designs of the engineered microsphere, respectively.

Taking the propagation direction or optical axis along the Z axis, the XY and YZ planes of measured light field intensity distributions are displayed in Fig. 5. As discussed in Fig. 4, the two-segment design produces two beams traveling in a twisted manner before they meet at the second focus. At the XY plane of the optical trap region, the trace of two beams is still obvious, and thus the transverse plane intensity distribution is not uniform. As displayed in Fig. 5(b), the cross section of the optical trap possesses an elliptical shape null at the center. Transverse dimensions are $\sim 600\ \text{nm}$ in the major axis and $300\ \text{nm}$ in the minor axis, respectively. However, for the measured XY plane result in Fig. 5(c), it seems the optical null from the fabricated sample is less flattening or elliptic, as it displays a dimension of $\sim 700\ \text{nm}$ along the major axis and $\sim 500\ \text{nm}$ along the minor axis. This might be due to the fact that the hexagonal copper TEM mesh grid holding the microsphere has a smaller diameter ($\sim 19\ \mu\text{m}$) than the microsphere (diameter $22.0\ \mu\text{m}$). This results in an effectively smaller entrance aperture that partially obstructs some off-axis illumination light. Such a portion of light, if not obstructed, can be directed by the microsphere and its patterned surface to focus close to the optical axis at this observation plane and contributes to the simulated elliptical shape of the optical null. Observing the YZ plane results, the experimentally measured light field in Fig. 5(f) shows most

of the key features presented in Fig. 5(e) with similar spatial positions.

Figures 6(a) and 6(d) display the SEM and optical images of the fabricated four-segment design microsphere. From Fig. 3, the four-segment design creates phase nulls in the transverse plane between the two foci. As such, the transverse plane intensity distribution is more uniform within the 3D optical trap region. As demonstrated in Fig. 6(b), the cross section of the optical trap possesses a round-shape null at the center with a diameter of $\sim 400\ \text{nm}$, while the measured XY plane result in Fig. 6(c) also shows that a round-shape optical null is generated from the four-segment sample, which largely agrees with the simulation. Nevertheless, the actual diameter of the generated optical trap at the same plane is $\sim 490\ \text{nm}$. As mentioned above, the engineered microspheres are sitting on a copper TEM grid with a mesh size ($\sim 19\ \mu\text{m}$) slightly smaller than the microsphere diameter, resulting in an effective entrance aperture to partially restrict off-axis illumination. The enlarged sizes could also be due to background interference with deflected light from neighboring mesh grids. Observing the YZ plane results, the experimentally measured light field in Fig. 6(f) shows most of the key features presented in Fig. 6(e) with similar spatial positions.

Both fabricated samples produce sub-wavelength size optical nulls that can be used to trap nanoparticles in 3D space. For 3D trapping of cold single atoms, a conventional method is to use holography to create bottle beams, in which the smallest trap size achieved is $\sim 2\ \mu\text{m}$ in the radial direction, and the axial size

is about twice that of the radial one [42]. As a comparison, our approach provides even smaller trap dimensions in both the axial and radial directions. However, it can be seen from both figures that in the measured light fields, the 3D void space part has the enclosure light field generally larger in size, and its connection to the two foci in the axial directions is weaker. In this sense, the actual laser power threshold required for trapping a nanoparticle in position is larger than that being designed. One way to improve the experimental condition is to change the holding substrate from metallic mesh grids to a transparent substrate to reduce background interference.

4. CONCLUSIONS

This paper proposes a novel scheme of the engineered microsphere with the segmented regions of diffractive patterns to generate an optical bottle beam with specially manipulated wavevectors under linearly polarized illuminations (wavelength of 532 nm). The emitted light field from the exit surface of the engineered microsphere forms a pair of axially arranged focused beams, and they are connected with a continuous optical field embracing a 3D optical null or void at the center. Such a new design can be executed into different embodiments, two such designs are demonstrated with both simulation and experiment. The two-segment design is simpler, but the intensity field distribution around the optical null is less uniform, while the four-segment design creates a 3D optical trap with more uniform intensity field. This novel scheme paves a way to create new micro-optics for specialized functional light field generation, which can be tuned by changing parametric designs, including the etched groove depth and total relative dislocations of centers of curvature. Further tuning can be possible if more types of diffraction patterns (e.g., photon sieves) are included in the segmented region design. Other than localized 3D optical trapping, this class of design can be used in the applications of structured light illumination microscopy and laser micro-processing.

Funding. Ministry of Education—Singapore (MOE2019-T2-2-147).

Disclosures. The authors declare no conflicts of interest.

REFERENCES

1. A. Ashkin, "Acceleration and trapping of particles by radiation pressure," *Phys. Rev. Lett.* **24**, 156–159 (1970).
2. M. Daly, M. Sergides, and S. Nic Chormaic, "Optical trapping and manipulation of micrometer and submicrometer particles," *Laser Photon. Rev.* **9**, 309–329 (2015).
3. A. Ashkin, J. M. Dziedzic, J. E. Bjorkholm, and S. Chu, "Observation of a single-beam gradient force optical trap for dielectric particles," *Opt. Lett.* **11**, 288–290 (1986).
4. K. Dholakia, P. Reece, and M. Gu, "Optical micromanipulation," *Chem. Soc. Rev.* **37**, 42–55 (2008).
5. J. M. Zhu, X. Q. Zhu, Y. F. Zuo, X. J. Hu, Y. Shi, L. Liang, and Y. Yang, "Optofluidics: the interaction between light and flowing liquids in integrated devices," *Opto-Electron. Adv.* **2**, 19000701 (2019).
6. W. Liu, D. S. Dong, H. Yang, Q. H. Gong, and K. B. Shi, "Robust and high-speed rotation control in optical tweezers by using polarization synthesis based on heterodyne interference," *Opto-Electron. Adv.* **3**, 200022 (2020).
7. E. Otte and C. Denz, "Optical trapping gets structure: structured light for advanced optical manipulation," *Appl. Phys. Rev.* **7**, 041308 (2020).
8. C. Bradac, "Nanoscale optical trapping: a review," *Adv. Opt. Mater.* **6**, 1800005 (2018).
9. A. Constable, J. Kim, J. Mervis, F. Zarinetchi, and M. Prentiss, "Demonstration of a fiber-optical light-force trap," *Opt. Lett.* **18**, 1867–1869 (1993).
10. C. Liberale, P. Minzioni, F. Bragheri, F. De Angelis, E. Di Fabrizio, and I. Cristiani, "Miniaturized all-fiber probe for three-dimensional optical trapping and manipulation," *Nat. Photonics* **1**, 723–727 (2007).
11. Y. Liu and M. Yu, "Investigation of inclined dual-fiber optical tweezers for 3D manipulation and force sensing," *Opt. Express* **17**, 13624–13638 (2009).
12. A. Asadollahbaik, S. Thiele, K. Weber, A. Kumar, J. Drozella, F. Sterl, A. M. Herkommer, H. Giessen, and J. Fick, "Highly efficient dual-fiber optical trapping with 3D printed diffractive Fresnel lenses," *ACS Photon.* **7**, 88–97 (2020).
13. M. Plidschun, H. Ren, J. Kim, R. Förster, S. A. Maier, and M. A. Schmidt, "Ultrahigh numerical aperture meta-fibre for flexible optical trapping," *Light Sci. Appl.* **10**, 57 (2021).
14. S. Kawata and T. Tani, "Optically driven Mie particles in an evanescent field along a channeled waveguide," *Opt. Lett.* **21**, 1768–1770 (1996).
15. A. H. J. Yang, T. Lerdsuchatawanich, and D. Erickson, "Forces and transport velocities for a particle in a slot waveguide," *Nano Lett.* **9**, 1182–1188 (2009).
16. S. Yu, J. Lu, V. Ginis, S. Kheifets, S. W. D. Lim, M. Qiu, T. Gu, J. Hu, and F. Capasso, "On-chip optical tweezers based on freeform optics," *Optica* **8**, 409–414 (2021).
17. M. L. Juan, M. Righini, and R. Quidant, "Plasmon nano-optical tweezers," *Nat. Photonics* **5**, 349–356 (2011).
18. K. B. Crozier, "Quo vadis, plasmonic optical tweezers?" *Light Sci. Appl.* **8**, 35 (2019).
19. H. Tan, H. Hu, L. Huang, and K. Qian, "Plasmonic tweezers for optical manipulation and biomedical applications," *Analyst* **145**, 5699–5712 (2020).
20. Y. Y. Sun, X. C. Yuan, L. S. Ong, J. Bu, S. W. Zhu, and R. Liu, "Large-scale optical traps on a chip for optical sorting," *Appl. Phys. Lett.* **90**, 031107 (2007).
21. S. Lin, E. Schonbrun, and K. Crozier, "Optical manipulation with planar silicon microring resonators," *Nano Lett.* **10**, 2408–2411 (2010).
22. A. Krishnan, N. Huang, S.-H. Wu, L. J. Martínez, and M. L. Povinelli, "Enhanced and selective optical trapping in a slot-graphite photonic crystal," *Opt. Express* **24**, 23271–23279 (2016).
23. J. Airt and M. J. Padgett, "Generation of a beam with a dark focus surrounded by regions of higher intensity: the optical bottle beam," *Opt. Lett.* **25**, 191–193 (2000).
24. V. G. Shvedov, A. V. Rode, Y. V. Izdebskaya, A. S. Desyatnikov, W. Krolikowski, and Y. S. Kivshar, "Giant optical manipulation," *Phys. Rev. Lett.* **105**, 118103 (2010).
25. V. G. Shvedov, A. S. Desyatnikov, A. V. Rode, W. Krolikowski, and Y. S. Kivshar, "Optical guiding of absorbing nanoclusters in air," *Opt. Express* **17**, 5743–5757 (2009).
26. V. G. Shvedov, C. Hnatovsky, A. V. Rode, and W. Krolikowski, "Robust trapping and manipulation of airborne particles with a bottle beam," *Opt. Express* **19**, 17350–17356 (2011).
27. A. Khoroshun, A. Ryazantsev, O. Ryazantsev, S. Sato, Y. Kozawa, J. Masajada, A. Popiolek-Masajada, M. Szatkowski, A. Chernykh, and A. Bekshaev, "Formation of an optical field with regular singular-skeleton structure by the double-phase-ramp converter," *J. Opt.* **22**, 025603 (2020).
28. L. Chen, Y. Zhou, M. Wu, and M. Hong, "Remote-mode microsphere nano-imaging: new boundaries for optical microscopes," *Opto-Electron. Adv.* **1**, 170001 (2018).
29. L. Chen, Y. Zhou, Y. Li, and M. Hong, "Microsphere enhanced optical imaging and patterning: from physics to applications," *Appl. Phys. Rev.* **6**, 021304 (2019).
30. B. S. Luk'yanchuk, Z. Wang, W. Song, and M. Hong, "Particle on surface: 3D-effects in dry laser cleaning," *Appl. Phys. A* **79**, 747–751 (2004).

31. B. S. Luk'yanchuk, R. Paniagua-Domínguez, I. V. Minin, O. V. Minin, and Z. Wang, "Refractive index less than two: photonic nanojets yesterday, today and tomorrow [Invited]," *Opt. Mater. Express* **7**, 1820–1847 (2017).
32. M. X. Wu, B. J. Huang, R. Chen, Y. Yang, J. F. Wu, R. Ji, X. D. Chen, and M. H. Hong, "Modulation of photonic jets generated by microspheres decorated with concentric rings," *Opt. Express* **23**, 20096–20103 (2015).
33. M. Wu, R. Chen, J. Ling, Z. Chen, X. Chen, R. Ji, and M. Hong, "Creation of a longitudinally polarized photonic jet via an engineered microsphere," *Opt. Lett.* **42**, 1444–1447 (2017).
34. Y. Zhou, H. Gao, J. Teng, X. Luo, and M. Hong, "Orbital angular momentum generation via a spiral phase microsphere," *Opt. Lett.* **43**, 34–37 (2018).
35. Y. Zhou, R. Ji, J. Teng, and M. Hong, "Wavelength-tunable focusing via a Fresnel zone microsphere," *Opt. Lett.* **45**, 852–855 (2020).
36. Y. Zhou, R. Ji, J. Teng, and M. Hong, "Ultralong light focusing via negative axicon microsphere," *Eng. Res. Express* **2**, 015044 (2020).
37. Y. Zhou and M. Hong, "Formation of polarization-dependent optical vortex beams via an engineered microsphere," *Opt. Express* **29**, 11121–11131 (2021).
38. V. N. Mahajan, *Aberration Theory Made Simple* (SPIE, 1991).
39. A. Mikš and J. Novák, "Third-order aberration coefficients of a thick lens," *Appl. Opt.* **51**, 7883–7886 (2012).
40. M. Born and E. Wolf, *Principles of Optics*, 7th ed. (Cambridge, 1999).
41. Y. Zhang, H. An, D. Zhang, G. Cui, and X. Ruan, "Diffraction theory of high numerical aperture subwavelength circular binary phase Fresnel zone plate," *Opt. Express* **22**, 27425–27436 (2014).
42. D. Barredo, V. Lienhard, P. Scholl, S. de Léséleuc, T. Boulier, A. Browaeys, and T. Lahaye, "Three-dimensional trapping of individual Rydberg atoms in ponderomotive bottle beam traps," *Phys. Rev. Lett.* **124**, 023201 (2020).